

Continuous wave operation of terahertz quantum cascade wire lasers with dual coupled gratings

TAN Cheng^{1,2}, ZOU Ting-Ting^{1,2}, ZANG Shan-Zhi^{1,2}, WANG Kai¹, GAN Liang-Hua¹, CAO Chen-Tao³, CHEN Bing-Qi³, CHEN Hong-Tai³, ZHANG Yue-Heng⁴, FANG Yu-Long^{3*}, XU Gang-Yi^{1,5*}

- (1. National Key Laboratory of Infrared Detection Technologies, Shanghai Institute of Technical Physics, Chinese Academy of Sciences, Shanghai 200083, China;
2. University of Chinese Academy of Sciences, Beijing 100049, China;
3. Hebei Semiconductor Research Institute, Shijiazhuang 050051, China;
4. School of Physics and Astronomy, Shanghai Jiao Tong University, Shanghai 200083, China;
5. College of Physics and Optoelectronic Engineering, Hangzhou Institute for Advanced Study, University of Chinese Academy of Sciences, Hangzhou 310024, China)

Abstract: We demonstrate terahertz quantum cascade (THz-QC) wire lasers based on dual coupled gratings that achieve continuous-wave (CW) operation near liquid nitrogen temperatures with a low-divergence Gaussian-like beam profile. Our configuration circumvents the effective refractive index constraint, significantly enhancing fabrication efficiency while retaining the key advantages of low power consumption and high heat dissipation efficiency. By engineering the photonic band structure of the coupled gratings, the laser operates on two supermodes. For Supermode #1, grating 1 serves as the master oscillator while grating 2 functions as a phased antenna array, featuring a collimated beam. For Supermode #2, grating 2 is the main oscillator and simultaneously provides a collimated beam, while grating 1 offers high reflectivity. Both supermodes exhibit high cavity quality factors and low beam divergence, achieved with a significantly reduced gain area. Experimentally, both supermodes are observed, and the optimized laser produces a collimated Gaussian beam with divergence angles of $12^\circ \times 18^\circ$ and an optical power of 1.04 mW. The threshold power consumption and thermal resistance are as low as 2.62 W and 8.5 mK/W/cm², respectively, resulting in a maximum CW operating temperature of 78.0 K. This work offers a more accessible route for low-divergence, low-power-consumption, high-thermal-dissipation-efficiency THz-QCLs with enhanced CW operation at elevated temperatures.

Key words: terahertz, quantum cascade laser, grating, continuous-wave mode

连续波工作的耦合双光栅太赫兹量子级联线激光器

谭 诚^{1,2}, 邹婷婷^{1,2}, 臧善志^{1,2}, 王 凯¹, 甘良华¹, 曹晨涛³, 陈炳奇³, 陈宏泰³, 张月蘅⁴, 房玉龙^{3*}, 徐刚毅^{1,5*}

- (1. 中国科学院上海技术物理研究所 红外探测全国重点实验室, 上海 200083;
2. 中国科学院大学, 北京 100049;
3. 河北半导体研究所, 河北 石家庄 050051;
4. 上海交通大学 物理与天文学院, 上海 200083;
5. 国科大杭州高等研究院 物理与光电工程学院, 浙江 杭州 310024)

摘要: 本文提出一种基于耦合双光栅的太赫兹量子级联(THz-QC)线激光器, 其在液氮温度以上连续波(CW)模式工作并有低发散角的高斯型光束。器件采用窄脊宽的双金属(MM)波导, 用于降低功耗并提升散热效率。通过设计光栅的能带结构, 使激光器具有两个超模。超模1以光栅1作为主控震荡器, 光栅2作为相控天线阵列提

Received date: 2025-02-05, accepted date: 2025-04-01

收稿日期: 2025-02-05, 录用日期: 2025-04-01

Foundation items: Supported by the National Natural Science Foundation of China (12393833, 62235010, 62435020, 12274285)

Biography: TAN Cheng (1997—), male, Qingdao, PhD. Research area involves the terahertz quantum cascade laser. E-mail: tancheng@mail.stip.ac.cn

*Corresponding authors: E-mail: yulong@163.com, gangyi.xu@mail.stip.ac.cn

供准直的波束辐射;超模2以光栅2作为主控振荡器提供准直光束,光栅1提供高反射率。两超模均具有高的品质因子与小光束发散角,这能显著缩短腔长并降低功耗。通过实验,可以观察到两个超模,产生发散角为 $12^\circ \times 18^\circ$ 、光功率为1.04 mW的准直的高斯光束。器件阈值功耗与热阻分别低至2.62 W与8.5 mK/W/cm²,最高CW工作温度为78.0 K。本文深入研究了耦合双光栅系统中模式调控的机制,并为实现小发散角、低功耗、高散热效率的太赫兹量子级联激光器(THz-QCL)提供了更易达成的途径,并使之在更高温度下的CW模式工作时具有更好的性能。

关键词: 太赫兹;量子级联激光器;光栅;连续模式

中图分类号: O43

文献标识码: A

Introduction

Terahertz quantum cascade lasers (THz-QCLs) hold significant promise for applications in precision spectral analysis^[1-3], terahertz real-time imaging^[4-6], high-speed communications^[7-9], astronomy^[10-12], etc. Most of these applications demand extremely high spectral precision, which requires THz-QCLs to operate in continuous-wave (CW) to suppress current and temperature fluctuations. Although near-room-temperature pulsed operation has been achieved recently, CW operation of THz-QCLs remains at cryogenic temperatures. This limitation arises from high power consumption and inefficient heat dissipation in the active region. Currently, THz-QCLs typically exhibit power consumption density exceeding 1×10^7 W/cm³, but the intrinsic vertical thermal conductivity of the active region is as low as $9.6T^{0.14}$ W/m/K^[13]. Therefore, thermal management must be carefully considered in the design of the active region and laser cavity.

Achieving a low threshold current density is the long-standing challenge of the design of active region, and the main task is to suppress the depopulation of the upper laser level (ULL) via electron-LO phonon scattering, the thermal excitation of electrons from ULL to the continuum, and the leakage current channels through parasitic energy levels^[14]. Recently, Q. Hu et al. proposed a double-well structure that suppressed leak current by eliminating parasitic energy levels, enabling pulsed operation near room temperature^[15]. It may lead to a new solution to improve the CW operation temperature (T_{CW}).

To improve T_{CW} and maintain favorable power characteristics and beam quality, the design of the laser cavity must address electromagnetic (EM) field confinement, quality factor, and thermal management. Low power consumption typically necessitates a small pumping area, often at the expense of EM confinement, threshold, and beam quality. Balancing heat dissipation, field confinement, and beam quality has led to the development of several innovative resonator configurations, including micro-cavity^[16], photonic crystals^[17-20], VECSEL^[21], and wire lasers^[14].

Among these, wire lasers-whose ridge width is much less than the free space wavelength - are particularly promising because of their high optical confinement factor, low threshold, and low power consumption. Notably, the effective heat dissipation area in wire lasers is substantially larger than the heat generation area, a criti-

cal factor for T_{CW} . However, traditional edge-emitting wire lasers, such as Fabry-Pérot (FP) lasers, feature a deep-subwavelength aperture, resulting in low power collection efficiency and highly divergent beams^[22, 23].

In order to improve the power extraction and beam quality, Amanti et al. first proposed a third-order DFB THz-QC wire laser^[24, 25]. The strong optical feedback significantly decreases the cavity length and thus reduces the power consumption. More importantly, by adjusting the effective refractive index (n_{eff}) very close to 3, the DFB grating acts as a phased array of end-fired antennas and results in a compact beam. Based on that work, more judiciously designed third-order DFB wire lasers have been realized, including perfectly phase-matched third-order DFB lasers^[26], phased arrays of antenna-coupled third-order DFB lasers^[27], antenna-coupled photonic line lasers^[28] and unidirectional photonic line lasers^[29]. The record-high T_{CW} of 129.0 K has been achieved with third-order DFB wire lasers, with a divergence angle of $33^\circ \times 22.5^\circ$ ^[30]. However, tailoring the effective index of the waveguide close to 3 imposes a challenging requirement on device fabrication. Therefore, it is highly desired to innovate laser cavities that leverage the excellent thermal management of wire lasers while enhancing the robustness and feasibility of fabrication^[31].

In this paper, we proposed and realized a novel wire laser configuration based on dual coupled gratings as the cavity. By tuning the photonic energy band structure of the two coupled gratings, as experimentally proved, the lasers operate on two candidate supermodes. In Supermode #1, grating 1 (G_1) operates in TM₀₀ first-order DFB mode at 3.24 THz, while grating 2 (G_2) functions as a phased array, providing high beam quality. In Supermode #2, G_2 operates in the TM₀₁ third-order DFB mode at 3.55 THz, producing a collimated beam, while G_1 provides high reflectivity to reduce the threshold. Such configuration relaxes the requirement of the effective index of the waveguide, and thus greatly improves the manufacturing friendliness and design flexibility. In addition, the lasers exhibit a collimated beam profile, a low threshold, and ultimately a high T_{CW} .

1 Design

The active region exploited in this work incorporates a bound-to-continuum structure^[32], with a gain spectra spanning approximately from 3.0 THz to 3.8 THz. Figure 1 (a) shows a schematic of the wire laser, which is based on a metal-metal (MM) waveguide, namely, the

active region is directly sandwiched between the top and bottom metallization. The width of the wire laser is as low as 40 μm , greatly reducing the heat generation but facilitating the heat dissipation. There are two gratings, G_1 and G_2 , patterned end-to-end on the top metallization, each of which consists of periodic air slits in the metallic layer with distinct parameters including the period length (A_i , $i = 1, 2$), the metal duty cycle (η_i), and the number of periods (N_i). The goal of coupled two gratings is to construct low-loss, low-consumption, and low-divergent supermodes, all of which are crucial for high T_{CW} . In addition, unpumped lead area and absorbing boundaries are formed on the both ends. It is worth noting that, such device configuration avoids the deep dry etching of deep-sub-wavelength patterns—commonly used in previously reported THz wire lasers^[28, 29]—and thus greatly simplifies the device fabrication.

According to the gain spectrum, A_1 , η_1 and N_1 are set as 13.9 μm , 75.0%, and 25 for G_1 , and A_2 and η_2 are 43.1 μm and 76.8% for G_2 while several different N_2 are investigated. Here, the gap between the two gratings is set approximately as the effective wavelength in the waveguide, ensuring efficient EM field transition between the two gratings. The grating structures and the resultant behavior of the relevant supermodes root from the photonic band structure of the individual gratings, as respectively shown in Figs. 1(b) and 1(c). Here, the photonic band structures are calculated by means of the full-wave finite element method (FEM) with a commercial package of COMSOL Multiphysics.

Figure 1(b) shows that, in the frequency range of gain spectrum, G_1 exhibits 2 high- Q_{cav} band-edge modes, both featuring fundamental EM field distributions in both the transversal and the longitudinal directions. Here, Q_{cav} refers to the cavity quality factor, accounting for both radiation loss and field leakage. The high-frequency band-edge mode at 3.79 THz is not considered due to the significant gain reduction at the high-frequency tail of the

gain spectrum. In contrast, the low-frequency mode at 3.24 THz, corresponding to the first-order DFB mode, is of particular interest as it is located near the center of the gain spectrum. However, this mode lies well below the light line (marked by the blue line in Fig. 1(b)), and therefore cannot radiate directly into free space. In turn, Fig. 1(c) depicts the band structure of G_2 , where the TM_{00} and TM_{01} modes are marked in black and red, respectively. Here, the TM_{01} mode features a node of EM field in the center of the waveguide along the y -direction. Among all the band-edge modes, the TM_{01} third-order DFB mode at 3.55 THz is the most relevant. Positioned near the center of the gain spectrum, this mode benefits from the peak material gain and exhibits the highest Q_{cav} among all modes. Furthermore, its frequency lies just above the light line, enabling the radiation into the free space via grazing emission.

The coupling between the two gratings significantly modulates the field distribution and ultimately leads to two high- Q_{cav} supermodes. Figures 2(a) and 2(b) respectively show the simulated EM field distribution of these two supermodes in an exemplar configuration, where N_2 equals to 10. Figure 2(a) illustrates that Supermode #1 ($f_1 = 3.24$ THz) originates from the band-edge mode of G_1 for its high Q_{cav} -factor ($Q_{\text{cav}} = 274$, when $N_2 = 10$). A portion of the field leaks out of G_1 and propagates into G_2 , where it oscillates as the low- Q_{cav} mode of the latter (indicated by the green dot in Fig. 1(c)). Note that Supermode #1 is located below the light line of G_1 but slightly above the light line of G_2 . Consequently, G_1 operates as the master oscillator and G_2 as a grating coupler that diffracts the EM field into free space. Indeed, the air slits in G_2 can be treated as a phased antenna array, creating an arc-shaped far-field distribution with an acute emission angle (θ_y). In the ideal case of grazing emission from an infinite array, with the frequency located on the light line, θ_y equals to zero and the arc-shaped beam evolves into a non-divergence Gaussian beam. In reality,

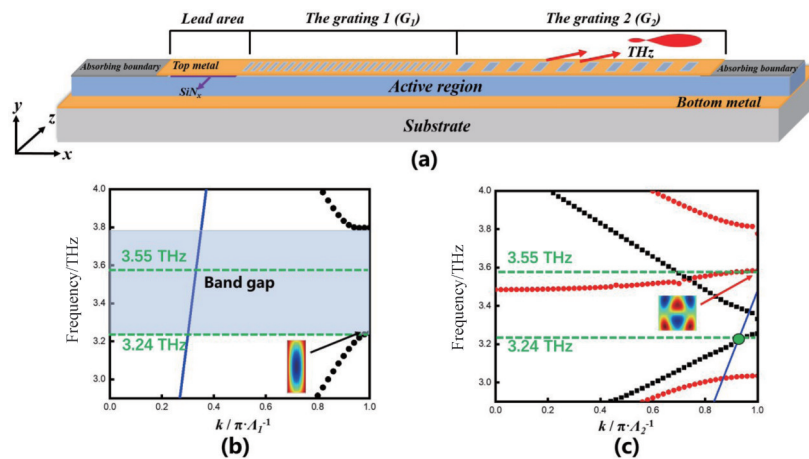


Fig. 1 (a) 3D schematic of the dual-coupled grating laser, featuring the absorbing boundary, lead area, and gratings; (b) simulated photonic band structure of G_1 ($A_1 = 13.9$ μm , $\eta_1 = 75.0\%$) and (c) G_2 ($A_2 = 43.1$ μm , $\eta_2 = 76.8\%$), where the light line is indicated in blue, the TM_{00} mode in black, and the TM_{01} mode in red, Supermodes #1 and #2 are represented by green dashed lines

图1 (a)耦合双光栅激光器的三维示意图,其包含吸收边界、引线区和光栅;(b)计算得到 G_1 ($A_1 = 13.9$ μm , $\eta_1 = 75.0\%$)和(c) G_2 ($A_2 = 43.1$ μm , $\eta_2 = 76.8\%$)的光子带结构,其中光线用蓝色标出, TM_{00} 模式用黑色标出, TM_{01} 模式用红色标出,超模1和超模2用绿色虚线标出

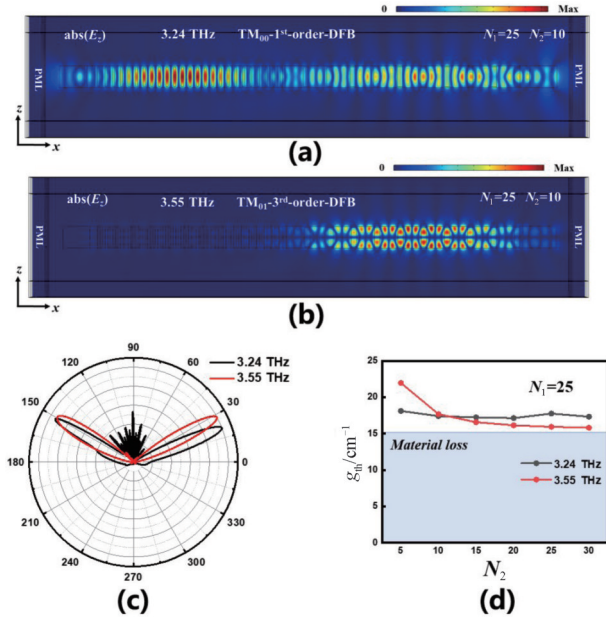


Fig. 2 (a) E_z -field distribution of Supermode #1 (3.24 THz), with the EM field primarily concentrated in G_1 ; (b) E_z -field distribution of Supermode #2 (3.55 THz), with the majority of EM field oscillating in G_2 ; (c) two-dimensional far-field distribution of Supermode #1 and Supermode #2 in x - y plane at $N_2=10$, with the emission angles θ_y of 22° and 29°, and the divergence angles of 15° and 16°, respectively; (d) threshold (g_{th}) trends as a function of N_2 for both supermodes, with the intrinsic material loss (15 cm^{-1}) indicated by shading

图2 (a)超模1(3.24 THz)的 E_z 场分布,其电场分布集中在 G_1 中;(b)超模2(3.55 THz)的 E_z 场分布,其电场分布集中在 G_2 中;(c) $N_2=10$ 时,超模1和超模2在 x - y 平面内的二维远场分布,出射角(θ_y)分别为22°和29°,其发散角分别为15°和16°;(d)超模1和超模2阈值增益 g_{th} 随 N_2 的变化趋势,其中本征材料损耗(15 cm^{-1})由阴影标注

the deviation of the period length, the finite number of air silts, and the unperfected phase relation between the air slits make θ_y deviate from zero, and degrade the beam collimation. The simulation presented in Fig. 2(c) indicates that when $N_2=10$, the emission angle θ_y and divergence angle of Supermode #1 are 22° and 15° (in x - y plane), respectively.

Figure 2(b) reveals that Supermode #2 ($f_2 = 3.55 \text{ THz}$, $Q_{cav} = 1056$) arises from the TM_{01} third-order DFB band-edge mode of G_2 , as its field is predominantly localized within G_2 . Since f_2 lies within the photonic band gap of G_1 , the latter acts as a high-reflectivity mirror and thus reduces the threshold of Supermode #2. On the other hand, since Supermode #2 is slightly above the light line, it also exhibits grazing emission and produces a collimated beam. As shown in Fig. 2(c), when $N_2=10$, the emission angle θ_y and the beam divergence angle of Supermode #2 are 29° and 16° (in x - y plane), respectively. As N_2 increases, both the emission angle and the divergence angle decrease, approaching the ideal grazing emission.

Figure 2(d) shows the threshold gain (g_{th}) as a function of N_2 for the two supermodes. Here, g_{th} is calculated as $g_{th} = (\alpha_{mat} + \alpha_{cav})/I$, where I is the optical con-

finement factor, α_{mat} is the intrinsic material loss caused by Ohmic losses in the metallic layers and free carrier absorption in the active region, and $\alpha_{cav} = 2\pi n_{eff}/(\lambda \times Q_{cav})$ is the cavity loss. Here, n_{eff} is the effective index of the waveguide, and λ is the wavelength. In our devices, α_{mat} is approximated as a constant ($\sim 15.0 \text{ cm}^{-1}$). Figure 2(d) illustrates, thanks to the high Q_{cav} achieved, the cavity loss is much less than the intrinsic material loss α_{mat} . In addition, g_{th} is insensitive to N_2 for Supermode #1, but gradually decreases with N_2 for Supermode #2. This tendency is closely related to the field distribution of the two supermodes. When $N_2 \leq 10$, g_{th} of Supermode #1 is slightly lower than that of Supermode #2, while for $N_2 > 10$, the trend is reversed.

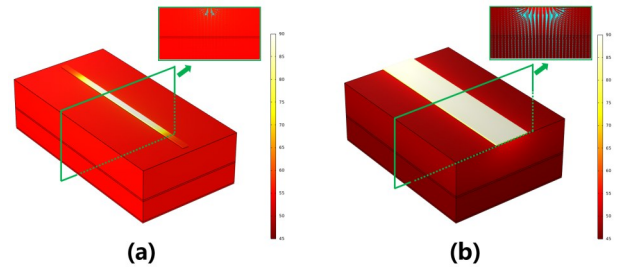


Fig. 3 Temperature distribution of (a) wire laser ($N_1=25$, $N_2=10$) and (b) conventional FP cavity (cavity length is 1 mm, ridge width is 200 μm) in CW mode at an average temperature of 77.0 K in the active region, the inset shows the temperature distribution at the cross-section indicated by the green box, with the cyan arrows representing the conduction heat fluxes, the length of the arrows is directly proportional to the magnitude of the heat fluxes

图3 有源区平均温度77.0 K,连续模式下,(a)线激光器($N_1=25$, $N_2=10$)与(b)传统FP腔(腔长为1 mm,脊宽为200 μm)的温度分布图,其中插图为绿色框所示截面处的温度分布,青色的箭头代表了传导热通量,其长度正比于热通量大小

We further calculated the area-normalized thermal resistance (R_{therm}) of the wire laser and the conventional wide-ridge FP THz QCL. R_{therm} is defined as $R_{therm} = \Delta T/P_{th}$, quantifying the heat dissipation performance of the laser and is crucial to the CW operation temperature T_{CW} . Here, ΔT is the temperature difference between the active region (T_{AR}) and the heat sink (T_{HS}), P_{th} is the threshold power density. To this aim, we first measured the threshold power density as a function of the heat sink temperature in pulsed mode with a duty cycle as low as 1%, where the heat accumulation in the active region is negligible, and thus $T_{AR} \approx T_{HS}$. In this way, we obtained the relationship between T_{AR} and P_{th} , which holds in both pulsed and CW operations. As shown in the next section, for a typical laser, when T_{AR} is 77.0 K, the threshold current density J_{th} is 450 A/cm² and P_{th} is $3.5 \times 10^6 \text{ W/cm}^3$. With these inputs, we calculated-in CW operation-the temperature distribution and the conducted heat flux in a 40 μm -wide wire laser and a 200 μm -wide FP laser, and the results are presented in Figs. 3(a) and 3(b), respectively. The calculated ΔT and R_{therm} are respectively 22.0 K and 6.4 mK/W/cm² for the wire laser, and 32.2 K and 9.4 mK/W/cm² for the wide ridge FP laser.

The considerably reduced thermal resistance of the wire laser roots from the more efficient lateral thermal conduction. The calculation shows that the lateral conducted heat flux is about 29.1% for the wire laser, compared to 23.6% for the wide-ridge FP laser, as shown in the insets.

2 Experiment

Based on the analyses above, three wire lasers are prepared with $N_2 = 10, 15, 25$, and named as laser A, B and C. The fabrication follows the standard THz MM waveguide process^[33,34]. Initially, Ti (10 nm)/Au (500 nm) layers were first evaporated on the surface of the epitaxial wafer and another n^+ GaAs carrier substrate. The epitaxial wafer was then inverted and bonded to the carrier substrate using Au/Au bonding. Mechanical milling and selective etching were employed to remove the substrate for epitaxy. So far, the active region was transferred to the carrier substrate, with the metallic layer serving as the lower electrode. Next, the 400 nm-thick n^+ GaAs cap laser was etched away except in the region of absorption boundaries. After that, a 200 nm-thick SiN_x film was deposited on the surface of the active region. Lithography and inductively coupled plasma (ICP) etching were used to create the insulation lead regions. Following this, the top metallic layer with the designed grating structure was formed by lithography and e-beam evaporation processes. The laser was then packaged, led, and mounted on the cold finger of a close-cycle cryostat for measurements. Figure 4(a) presents the SEM image of a typical wire laser and the zoomed-in views of the two gratings G_1 and G_2 . The area outlined by the white dashed line corresponds to the lead region.

In CW mode and at a heatsink temperature of 20.0 K, we first measured the lasing spectra of the three lasers at different injected currents. As shown in Figs. 4(b) to 4(d), all lasers predominantly operate on two modes at frequencies 3.24 THz and 3.55 THz, which perfectly

align with the simulated frequencies of Supermodes #1 and #2. The only exception is the appearance of a weak lasing mode at 3.22 THz in laser C, likely due to the TM_{00} third-order DFB mode from G_2 , as it exhibits a relatively high Q_{cav} (212) when N_2 equals 25. Notably, the spectral behavior of the three lasers varies under different pumping conditions. For laser A, Supermode #1 dominates when the injected current is near the threshold, but is overtaken by Supermode #2 at high currents. Such phenomena can be explained by the above-mentioned simulations, *i. e.*, due to the weak spatial overlap of the two supermodes (Figs. 2(a-b)) and the gain non-uniformity^[35], the mode competition is weak. Although the calculated Q_{cav} of Supermode #1 is lower than that of Supermode #2, fabrication-induced variations in the gratings may cause the actual Q_{cav} to deviate from the simulations, reducing the difference in the radiation losses. Consequently, the radiation efficiencies of the two supermodes may become comparable. However, Supermode #2 has a larger effective pumped area than Supermode #1, which enables the intensity of the former to surpass the latter as the injection current increases. In contrast, the lasing spectra of lasers B and C are dominated by Supermode #2 in the whole laser dynamic range. The reason is that, with the increase of N_2 , as shown in Fig. 2(d), Supermode #2 exhibits a lower threshold, in addition to its large pumping area and collimated beam pattern.

The far-field beam patterns of the three lasers were measured and compared with the simulations. During measurements, the injector current densities are respectively 694.0 A/cm², 670.0 A/cm², and 561.0 A/cm² for lasers A to C, and the related lasing spectra are presented in Figs. 4(b) to 4(d). During the simulations, the intensity profiles of each supermode were first calculated by means of FEM and – according to its lasing spectra – the weighted summation gave rise to the normalized beam pattern of the related laser. Figures 5(a) to 5(c) show the measured beam patterns of the three lasers,

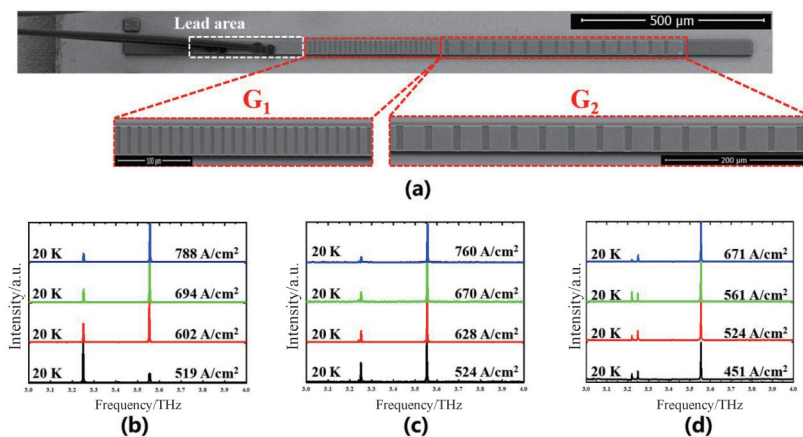


Fig. 4 (a) SEM image of laser B ($N_2 = 15$), including magnified views of G_1 , G_2 and the lead area, marked by a white dashed line; emission spectra of (b) laser A, (c) laser B and (d) laser C in 20.0 K CW mode, with varying injection current densities, the spectra show Supermode #1 (3.24 THz), Supermode #2 (3.55 THz) and a weak mode (3.22 THz), which only exists in laser C

图4 (a)激光器B的SEM图片,包括 G_1 和 G_2 的局部放大图和白色虚线标注的引线区;20.0 K连续模式下(b)激光器A,(c)激光器B和(d)激光器C,不同注入电流密度下的发射光谱,其包含了超模1(3.24 THz)和超模2(3.55 THz)与一个只在激光器C中出现的低强度的模式(3.22 THz)

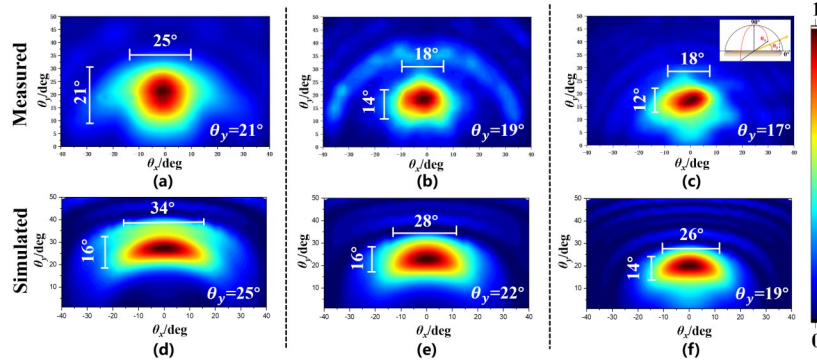


Fig. 5 Far-field distributions of (a) laser A, (b) laser B, and (c) laser C at current densities of 694.0 A/cm^2 , 670.0 A/cm^2 , and 561.0 A/cm^2 , with divergence angles of $21^\circ \times 25^\circ$, $14^\circ \times 18^\circ$, and $12^\circ \times 18^\circ$, and emission angles θ_y of 21° , 19° and 17° , respectively; following the weighted summation of the corresponding spectra, the simulated normalized beams of (d) laser A, (e) laser B and (f) laser C are obtained with divergence angles of $16^\circ \times 34^\circ$, $16^\circ \times 28^\circ$ and $14^\circ \times 26^\circ$, respectively, and the simulated exit angles are 25° , 22° and 19° , the inset shows the far-field measurement method

图5 (a)激光器A、(b)激光器B和(c)激光器C分别在电流密度为 694.0 A/cm^2 、 670.0 A/cm^2 和 561.0 A/cm^2 时的远场分布,其发散角分别为 $21^\circ \times 25^\circ$ 、 $14^\circ \times 18^\circ$ 和 $12^\circ \times 18^\circ$,其离去角(θ_y)分别为 21° 、 19° 和 17° ;按照对应光谱加权求和,得到(d)激光器A、(e)B和(f)C的模拟归一化光束的发散角分别为 $16^\circ \times 34^\circ$ 、 $16^\circ \times 28^\circ$ 和 $14^\circ \times 26^\circ$,得到的离去角分别为 25° 、 22° 和 19° ,插图为远场测量方式

while Figs. 5(d) to 5(f) show the simulated results. Figure 5 illustrates qualitative agreement between the experimental and simulated results, confirming that the two measured main modes originate from Supermodes #1 and #2. Interestingly, as N_2 increases from 10 to 25, the emission angle θ_y – indicated as inset of Fig. 5(c) – decreases from 21° to 17° , and the divergence angle reduces from $21^\circ \times 25^\circ$ to $12^\circ \times 18^\circ$, aligning closely with the antenna theory^[36]. These findings indicate that, increasing N_2 enhances beam collimation, a hallmark characteristic of wire lasers. The discrepancy between the experimental and simulated far-field profiles is likely caused by the limited collection angle of the optical path during the spectral measurement, which alters the rela-

tive intensity of the two supermodes and ultimately affects the simulated far-field profile of the mixed mode.

After identifying the origin of the lasing modes, we further investigated the light-current-voltage ($L-I-V$) and temperature characteristics in pulsed and CW operations. Figures 6(a-c) show the pulsed temperature-dependent $L-I-V$ curves for lasers A, B and C, respectively. In pulsed mode, the threshold current densities ($J_{th,pulsed}$) at 20.0 K are respectively 524.0 A/cm^2 , 476.0 A/cm^2 and 385.0 A/cm^2 for lasers A, B and C, and the related maximum operation temperatures (T_{pulsed}) are respectively 132.0 K, 136.0 K, and 137.0 K. Since, in pulsed mode (the pulse width is 1 μs , the repeat frequency is 10 kHz), the heat accumulation is neg-

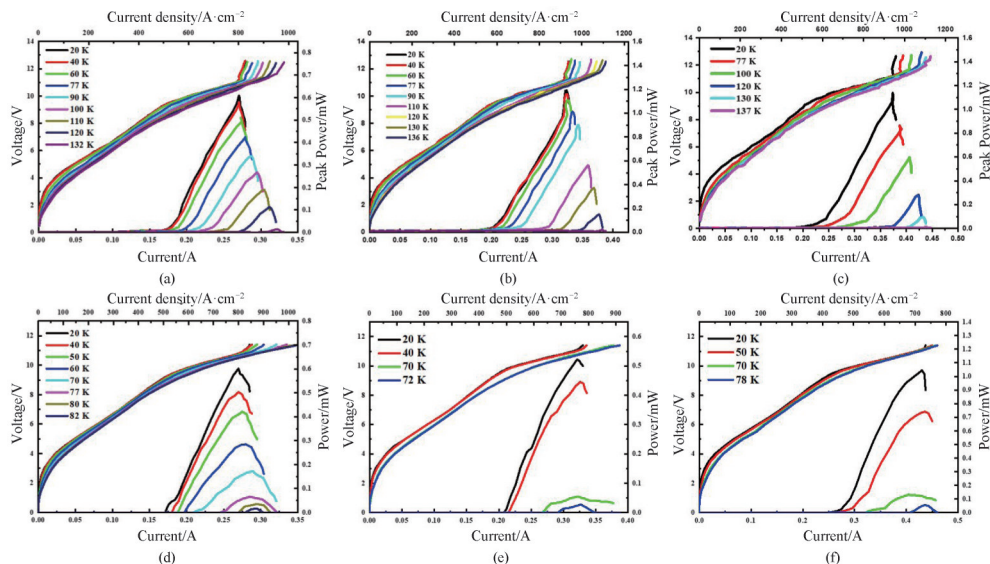


Fig. 6 (a), (b) and (c) show $L-I-V$ curves measured at different temperatures for laser A, laser B and laser C in pulsed mode, respectively, with the maximum T_{pulsed} of 132.0 K, 136.0 K and 137.0 K; (d), (e) and (f) show $L-I-V$ curves measured at different temperatures for laser A, laser B and laser C in CW mode, respectively, with the maximum T_{CW} of 82.0 K, 72.0 K and 78.0 K

图6 脉冲模式下(a)激光器A、(b)激光器B和(c)激光器C在不同温度下测得的 $L-I-V$ 曲线,最大 T_{pulsed} 分别为132.0 K、136.0 K和137.0 K; CW模式下(d)激光器A、(e)激光器B和(f)激光器C在不同温度下测得的 $L-I-V$ 曲线,最大 T_{CW} 分别为82.0 K、72.0 K和78.0 K

ligible, and the temperature of the active region equals approximately that of the heat sink. Therefore, the measured tendency is in qualitative agreement with the simulation, *i. e.*, the less threshold gain means the lower threshold current density and the higher operation temperature. Notably, the values of $J_{th,pulsed}$ and T_{pulsed} achieved in the wire lasers are comparable to that of the conventional wide-ridge FP lasers from the same material as we reported in Ref. [37]. These phenomena reflect that our novel cavity configuration does not cause obvious additional cavity loss compared to the long-cavity FP laser, which exhibits almost the lowest cavity loss in all tested cavity configurations^[38]. In addition, at 20.0 K, the peak output power increases from 0.6 mW for laser A to about 1.2 mW for lasers B and C, mainly due to the increase in pumping area.

Figures 6 (d-f) show respectively the temperature-dependent $L-I-V$ curves for lasers A, B and C, measured under the CW condition. At 20.0 K, the threshold current densities ($J_{th,cw}$) are respectively 512.0 A/cm², 493.2 A/cm² and 457.0 A/cm² for lasers A, B and C, keeping the same tendency as in the pulsed mode. Regarding the output power, the larger pumping area provides more gain for Supermode #2 as the simulations reveal, which leads laser C to achieve the highest power output of 1.04 mW among the three lasers. The maximum T_{cw} , a key indicator of thermal performance, is 82.0 K, 72.0 K, and 78.0 K for lasers A, B and C, respectively. It is worth emphasizing that the T_{cw} realized in the dual-grating wire lasers significantly exceeds those of the conventional wide-ridge FP lasers fabricated with the same material (49.5 K), as shown in Ref. [37].

Another notable phenomenon is that, despite having the highest threshold current density, laser A achieves the highest T_{cw} (82.0 K). Due to the different values of N_2 , the three lasers exhibit varying pumping areas, which are 33 740.0 μm^2 , 42 360.0 μm^2 and 59 600.0 μm^2 , respectively. Correspondingly, their threshold power consumptions are respectively 1.59 W, 2.04 W and 2.62 W, measured at 20.0 K. The results strongly suggest that, not only the threshold current density but the power consumption affects the achievable T_{cw} . To examine the influence of power consumption on heat dissipation, we estimated the values of R_{therm} of the three lasers

by comparing the relationship between the threshold current density and the heat sink temperature in pulsed and CW operations. Figure 7 (a) presents the variation of threshold current density as a function of heat sink temperature in pulsed and CW operations, respectively. In pulsed mode, the temperature of the active region is approximated to be the heat sink temperature. With the same threshold current density, the heat sink temperature under the CW condition is less than that under the pulsed condition, and the temperature difference is exploited to deduce the value of R_{therm} . The triangles in Fig. 7(a) illustrate a transformation from the CW to the pulsed characteristics using R_{therm} as the fitting parameter. In this way, R_{therm} is evaluated to be 4.0 mK/W/cm² for laser A. Figures 7 (b) and 7 (c) show the results of the other two lasers, and the related R_{therm} values are 5.0 mK/W/cm² and 8.5 mK/W/cm² for lasers B and C, respectively. In comparison to the conventional 130 μm -wide FP laser^[37], which has a R_{therm} of 18.5 mK/W/cm², the measured values of R_{therm} agree qualitatively to the calculated ones, taking into account the uncertainty of material thermal conductivity and the cooling power of the cryostat. The comparison among the three lasers indicates that the heat dissipation efficiency is related to not only the ridge width but also the cavity length, and the latter is often overlooked. Our work suggests that to improve the CW operating temperature, it is essential to minimize the threshold current density within the smallest possible gain area.

It is noteworthy that the T_{cw} and beam divergence realized in laser C is comparable to other state-of-the-art THz wire lasers, such as the unidirectional THz wire laser and the perfectly matched third-order DFB wire laser^[26, 29]. Nevertheless, the T_{cw} reported is still less than the record ever reported. We believe significant improvement of T_{cw} is expected in our laser configuration, by further decreasing the ridge width and modifying the structure parameters of the two coupled gratings to minimize the cavity length.

3 Conclusion

In conclusion, by eliminating the stringent requirements for the waveguide effective index and the demanding deep-etching technology, our novel laser configura-

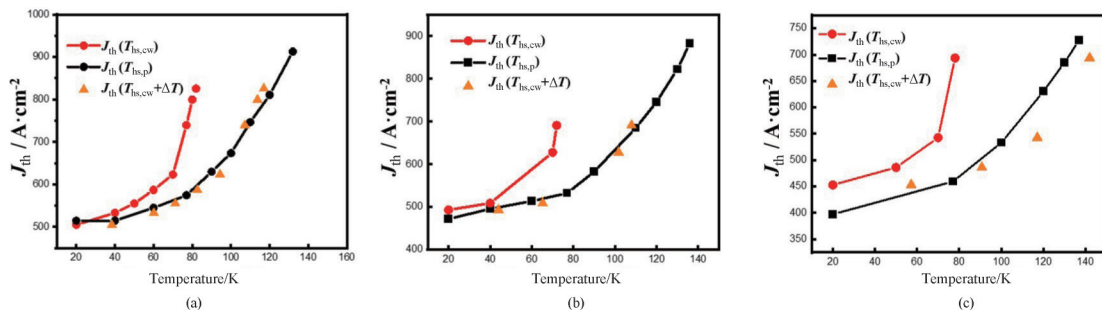


Fig. 7 Variation trends of the pulsed mode, CW mode and threshold current density after fitting using R_{therm} as a function of heat sink temperature for (a) laser A ($R_{therm} = 4.0$ mK/W/cm²), (b) laser B ($R_{therm} = 5.0$ mK/W/cm²) and (c) laser C ($R_{therm} = 8.5$ mK/W/cm²)

图7 (a)激光器A($R_{therm} = 4.0$ mK/W/cm²), (b)激光器B($R_{therm} = 5.0$ mK/W/cm²)和(c)激光器C($R_{therm} = 8.5$ mK/W/cm²)各自的脉冲模式、连续波模式和用 R_{therm} 拟合后的阈值电流密度随热沉温度的变化情况

tion achieves a collimated beam profile and an ultra-low power consumption while showcasing exceptional fabrication-friendly characteristics. The optimized laser demonstrates an output power of 1.04 mW in CW mode, featuring a Gaussian beam with a divergence angle of $12^\circ \times 18^\circ$ and a T_{CW} of 78.0 K. This work underscores the intricate EM field interactions in dual-coupled grating wire lasers and validates their outstanding thermal performance. Optimization strategies are given to improve T_{CW} , which can be summarized from both the optical and thermal perspectives. High T_{CW} operation requires a minimized threshold gain within a small pumping area and thus a lower power consumption. Also, the effective heat dissipation area needs to be significantly larger than the pumping area, which enhances the thermal conductivity.

Future efforts to fine-tune material properties and grating parameters could further optimize CW performance in terms of operation temperature, output power, and beam quality. These advancements would significantly broaden the application potential of the wire lasers.

References

- [1] Mitrofanov O, Renaud C C, Seeds A J. Terahertz probe for spectroscopy of sub-wavelength objects[J]. *Optics Express*, 2012, 20(6): 6197–6202.
- [2] Röben B, Lyu X, Biermann K, et al. Terahertz quantum-cascade lasers for high-resolution spectroscopy of sharp absorption lines[J]. *Journal of Applied Physics*, 2019, 125(15): 151613–1–151613–7.
- [3] Lyu X, Röben B, Biermann K, et al. Terahertz quantum-cascade lasers for high-resolution absorption spectroscopy of atoms and ions in plasmas[J]. *Semiconductor Science and Technology*, 2023, 38(3): 035003.
- [4] Hu Q. Terahertz quantum cascade lasers and real-time T-rays imaging at video rate[J]. *International Journal of High Speed Electronics and Systems*, 2008, 18(04): 983–992.
- [5] Hu B B, Nuss M C. Imaging with terahertz waves[J]. *Optics Letters*, 1995, 20(16): 1716–1718.
- [6] Lee A W M, Hu Q. Real-time, continuous-wave terahertz imaging by use of a microbolometer focal-plane array[J]. *Optics Letters*, 2005, 30(19): 2563–2565.
- [7] Fitch M J, Oslander R. Terahertz waves for communications and sensing[J]. *Johns Hopkins APL Technical Digest*, 2004, 25(4): 348–355.
- [8] Xu L, Curwen C, Reno J, et al. Terahertz metasurface quantum cascade lasers[C]. 2016 International Conference on Optical MEMS and Nanophotonics (OMN), IEEE, 2016: 1–2.
- [9] Nagatsuma T, Ducournau G, Renaud C C. Advances in terahertz communications accelerated by photonics[J]. *Nature Photonics*, 2016, 10(6): 371–379.
- [10] Kloosterman J L, Hayton D J, Ren Y, et al. Hot electron bolometer heterodyne receiver with a 4.7-THz quantum cascade laser as a local oscillator[J]. *Applied Physics Letters*, 2013, 102(1): 011123.
- [11] Hayton D J, Kloosterman J L, Ren Y, et al. A 4.7 THz heterodyne receiver for a balloon borne telescope[C]. *Millimeter, Submillimeter, and Far-Infrared Detectors and Instrumentation for Astronomy VII*, SPIE, 2014, 9153: 583–589.
- [12] Khalatpour A, Paulsen A K, Addamane S J, et al. A tunable unidirectional source for GUSTO's local oscillator at 4.74 THz[J]. *IEEE Transactions on Terahertz Science and Technology*, 2021, 12(2): 144–150.
- [13] Evans C A, Indjin D, Ikonik Z, et al. Thermal modeling of terahertz quantum-cascade lasers: comparison of optical waveguides[J]. *IEEE Journal of Quantum Electronics*, 2008, 44(7): 680–685.
- [14] Vitiello M S, Tredicucci A. Physics and technology of Terahertz quantum cascade lasers[J]. *Advances in Physics: X*, 2021, 6(1): 1893809.
- [15] Khalatpour A, Paulsen A K, Deimert G, et al. High-power portable terahertz laser systems[J]. *Nature Photonics*, 2021, 15(1): 16–20.
- [16] Fasching G, Tamosiunas V, Benz A, et al. Subwavelength microdisk and microring terahertz quantum-cascade lasers[J]. *IEEE Journal of Quantum Electronics*, 2007, 43(8): 687–697.
- [17] Diao Z, Bonzon C, Scalari G, et al. Continuous-wave vertically emitting photonic crystal terahertz laser[J]. *Laser & Photonics Reviews*, 2013, 7(5): L45–L50.
- [18] Klimont A, Ottomaniello A, Degl'Innocenti R, et al. Line-defect photonic crystal terahertz quantum cascade laser[J]. *Journal of Applied Physics*, 2019, 126(15): 153104–1–153104–8.
- [19] Liu J, Xu Y, Li R, et al. High-power electrically pumped terahertz topological laser based on a surface metallic Dirac-vortex cavity[J]. *Nature Communications*, 2024, 15(1): 4431.
- [20] Li R, Xu Y, Zhang S, et al. High brightness terahertz quantum cascade laser with near-diffraction-limited Gaussian beam[J]. *Light: Science & Applications*, 2024, 13(1): 193.
- [21] Xu L, Curwen C A, Reno J L, et al. High performance terahertz metasurface quantum-cascade VECSEL with an intra-cryostat cavity[J]. *Applied Physics Letters*, 2017, 111(10): 101101–1–101101–5.
- [22] Orlova E E, Hovenier J N, Klaassen T O, et al. Antenna model for wire lasers[J]. *Physical Review Letters*, 2006, 96(17): 173904.
- [23] Adam A J L, Kašalynas I, Hovenier J N, et al. Beam patterns of terahertz quantum cascade lasers with subwavelength cavity dimensions[J]. *Applied Physics Letters*, 2006, 88(15): 151105–1–151105–3.
- [24] Amanti M I, Scalari G, Castellano F, et al. Low divergence Terahertz photonic-wire laser[J]. *Optics Express*, 2010, 18(6): 6390–6395.
- [25] Amanti M I, Fischer M, Scalari G, et al. Low-divergence single-mode terahertz quantum cascade laser[J]. *Nature Photonics*, 2009, 3(10): 586–590.
- [26] Kao T Y, Hu Q, Reno J L. Perfectly phase-matched third-order distributed feedback terahertz quantum-cascade lasers[J]. *Optics Letters*, 2012, 37(11): 2070–2072.
- [27] Khalatpour A, Reno J L, Hu Q. Phase-locked photonic wire lasers by π coupling[J]. *Nature Photonics*, 2019, 13(1): 47–53.
- [28] Kao T Y, Cai X, Lee A W M, et al. Antenna coupled photonic wire lasers[J]. *Optics Express*, 2015, 23(13): 17091–17100.
- [29] Khalatpour A, Reno J L, Kherani N P, et al. Unidirectional photonic wire laser[J]. *Nature Photonics*, 2017, 11(9): 555–559.
- [30] Wienold M, Röben B, Schrotke L, et al. High-temperature, continuous-wave operation of terahertz quantum-cascade lasers with metal-metal waveguides and third-order distributed feedback[J]. *Optics Express*, 2014, 22(3): 3334–3348.
- [31] Biasco S, Garrasi K, Castellano F, et al. Continuous-wave highly-efficient low-divergence terahertz wire lasers[J]. *Nature Communications*, 2018, 9(1): 1122.
- [32] Amanti M I, Scalari G, Terazzi R, et al. Bound-to-continuum terahertz quantum cascade laser with a single-quantum-well phonon extraction/injection stage[J]. *New Journal of Physics*, 2009, 11(12): 125022.
- [33] Wang K, Bai H, Yu C, et al. Independent control of mode selection and power extraction in terahertz semiconductor lasers[J]. *ACS Photonics*, 2022, 9(6): 1973–1983.
- [34] Bai H Z, Zang S Z, Tan C, et al. Single mode terahertz quantum cascade lasers based on distributed Bragg reflector[J]. *J. Infrared Millim. Waves*, 2023, 42(6): 795–805.
- [35] 白弘宙, 臧善志, 谭诚, 等. 基于布拉格反射镜的单模太赫兹量子级联激光器[J]. *红外与毫米波学报*, 2023, 42(6): 795–805.
- [36] Burghoff D, Kao T Y, Ban D, et al. A terahertz pulse emitter monolithically integrated with a quantum cascade laser[J]. *Applied Physics Letters*, 2011, 98(6): 061112–1–061112–3.
- [37] Balanis C A. *Antenna theory: analysis and design*[M]. John Wiley & Sons, 2015.
- [38] Bai H, Liu G, Wang K, et al. Continuous-wave terahertz quantum cascade microlaser arrays operating on various bound states in the continuum[J]. *Optics Express*, 2023, 31(17): 27914–27926.
- [39] Yu C R. Mode selection and tailoration of the radiation efficiency in terahertz quantum cascade lasers[D]. University of Chinese Academy of Sciences (Shanghai Institute of Technical Physics, Chinese Academy of Sciences), 2020.
- [40] 俞辰初. 太赫兹量子级联激光器中模式选择与辐射效率的控制[D]. 中国科学院大学(中国科学院上海技术物理研究所), 2020.